

# **Tomographic resolution of ray and finite-frequency methods: a membrane-wave investigation**

**D. Peter<sup>1</sup>, L. Boschi<sup>1</sup> and J.H. Woodhouse<sup>2</sup>**

<sup>1</sup> *Institute of Geophysics, ETH Zurich, Hönggerberg HPP, CH-8093 Switzerland, Email: dpeter@erdw.ethz.ch*

<sup>2</sup> *University of Oxford, Department of Earth Sciences, Parks Road, Oxford OX1, 3PR, UK*

**Mai, 2008**

## **SUMMARY**

The purpose of this study is to evaluate the resolution potential of current finite-frequency approaches to tomography, and to do that in a framework similar to that of global scale seismology. According to our current knowledge and understanding, the only way to do this is by constructing a large set of “ground-truth” synthetic data computed numerically (spectral elements, finite differences, etc.), and then to invert them using the various available linearized techniques. Specifically, we address the problem of using surface wave data to map phase-velocity distributions. Our investigation is strictly valid for the propagation of elastic waves on a spherical, heterogeneous membrane, and, as shown by Peter *et al.* (2007), a good analogue for the propagation of surface waves within the outermost layers of the Earth. This amounts to drastically reducing the computational expense, with a certain loss of accuracy if very short-wavelength features of a strongly heterogeneous Earth are to be modeled. Our analysis suggests that a single-scattering, finite-frequency approach to tomography, with sensitivity kernels computed via the adjoint method, is significantly more powerful than ray-theoretic methods, as a tool to image the fine structure of the Earth.

21 **1 INTRODUCTION**

22 Surface waves propagate within the outermost shells of the Earth. While earthquakes and seismic  
 23 stations are non-uniformly distributed all over the globe, surface waves travel through remote re-  
 24 gions where no stations can be placed. They sample the Earth's upper mantle relatively uniformly.  
 25 Depending upon their frequency, surface waves are sensitive to different depth ranges in the man-  
 26 tle. For these reasons, observations of surface waves are a valuable source of information on the  
 27 global structure of the Earth. Many studies have been conducted to measure phase anomalies of  
 28 surface waves with respect to an *a priori* reference Earth (Trampert & Woodhouse 1995, 1996  
 29 and 2001; Laske 1995 and Laske & Masters 1996; Ekström *et al.* 1997; van Heijst & Woodhouse  
 30 1999). They lead to excellent databases of phase anomalies for surface waves with periods down  
 31 to approximately 35 s. The measurement techniques differ in the details (Trampert & Woodhouse  
 32 2001), but share the main principle, which consists of filtering the seismograms around a period  
 33 of interest within a narrow frequency band. The signal can also be decomposed into fundamental-  
 34 mode and overtones as well as arrivals for multiple orbits. Synthetic seismograms are computed  
 35 in a chosen, usually spherically symmetric, reference model. The phase anomalies are determined  
 36 with respect to such synthetic seismograms by cross-correlation or other fitting procedure (e.g., a  
 37 downhill-simplex algorithm as in Ekström *et al.* 1997).

38 An inverse problem can then be formulated, to determine the structure through which the sur-  
 39 faces waves travelled. Very large databases of phase-anomaly measurements are usually inverted  
 40 for local phase velocities, thus leading to global phase-velocity distributions, which are, to first or-  
 41 der, a linear combination of the underlying 3-D velocity structure. Before a seismic image is used  
 42 for geodynamical interpretation or other applications, its resolution must be known. The resolution  
 43 of tomography is influenced by many factors, e.g. by data coverage and measurement quality. It  
 44 is often investigated by so called checkerboard tests (Lévêque *et al.* 1993), solving for resolution  
 45 radii (e.g. Trampert & Woodhouse 1996) or by examining the full resolution matrices (e.g. Boschi,  
 46 2003; Boschi *et al.*, 2007). All these studies are limited, in that the approximate theory used to for-  
 47 mulate the inverse problem (ray theory) coincides with the theory used to compute synthetic data:  
 48 inaccuracies in the solution models resulting from inaccuracies in the approximate formulations of

wave propagation cannot be estimated (Lévêque *et al.* 1993). On the other hand, one can overcome this problem by computing synthetic data with a completely numerical forward approach. Unfortunately, for a fully realistic three-dimensional Earth model, this is very expensive to conduct (Qin *et al.* 2006), thus leading to a very limited amount of available synthetic data.

Concerning the theories involved in the formulation of the inverse problem, global tomography has mostly relied on ray theory due to its intuitive physical interpretation and computational efficiency. In practice, ray theory is valid when the wavelength of the seismic wave is much smaller than the scalelength of the heterogeneities the wave is traveling through. When inverting for a phase-velocity model, ray theory assumes that any perturbation of phase is due to a perturbation of local phase velocities located on the ray of the considered phase. Especially for surface waves at longer periods, further away from the regime where ray theory is valid, this approximation might limit significantly tomographic resolution. Single scattering of surface waves causes phase-anomaly measurements made over a finite-frequency band to be sensitive to phase-velocity perturbations distributed over large areas on the globe, and not only on the ray (Woodhouse & Girnus 1982; Li & Tanimoto 1993; Li & Romanowicz 1995; Dahlen *et al.* 2000; Hung *et al.* 2000; Spetzler *et al.* 2002; Zhou *et al.* 2004; Yoshizawa & Kennett 2005; Boschi 2006; Peter *et al.* 2007). These sensitivity areas, sometimes referred to as Born kernels (Marquering *et al.* 1999; Dahlen *et al.* 2000; Hung *et al.* 2000), are unique for every single measurement. In the presence of adequate data coverage, finite-frequency theory is expected potentially to reveal phase-velocity structures with spatial scalelengths smaller than the wavelength under consideration.

In the past, comparisons made between ray and finite-frequency theory have not decisively determined whether or not current formulations of finite-frequency theory improve the resolution of tomographic images. For example, Spetzler *et al.* (2002), Boschi (2006) and Peter *et al.* (2007) found that phase-anomaly observations for Love waves at intermediate to long periods were equally well inverted by rays and by Born kernels. The same can be deduced from Sieminski *et al.* (2004) at the regional scale, where a test with synthetically computed fundamental Rayleigh-wave data and a realistic distribution of events and stations suggested no improvement when using finite-frequency sensitivity kernels. On the other hand, Ritzwoller *et al.* (2002) inverted surface-wave

4    *Peter et al.*

77 group-velocity measurements for group velocity models and found a clear difference at all peri-  
78 ods between ray-theoretically and finite-frequency derived maps. Zhou *et al.* (2005) noted a slight  
79 improvement for finite-frequency theory as well, but limited to the case where three-dimensional  
80 sensitivity kernels were used to invert for seismic velocities directly, by-passing the derivation of  
81 phase-velocity maps. The statistical significance of such improvements remains to be determined.

82    In this study, we compare different tomographic algorithms based on ray theory versus single-  
83 scattering finite-frequency theory. In sections 2 and 3, we first consider the forward problem of  
84 predicting phase anomalies for a given phase-velocity model. In the first part of this study, we  
85 derive an asymptotic expression for membrane waves traveling on a sphere. This analytical ex-  
86 pression can further be used to calculate waveforms for heterogeneous background models, once  
87 the ray path between source and station is found. We validate phase-anomaly predictions made by  
88 exact ray theory and finite-frequency theory, comparing them with numerical “membrane-wave”  
89 results. In the second part of this study, we measure the accuracy of tomographic algorithms based  
90 on linearized ray-theory and finite-frequency tomography. The effects of scalelength, amplitude,  
91 noise and wavelength upon the imaging process are all specifically evaluated. In order to calculate  
92 synthetic data, we simplify the numerical approach by employing the membrane wave method to  
93 simulate nonlinear surface wave propagation effects for a laterally heterogeneous Earth. The syn-  
94 thetic databases are comparable in size to existing ones. We invert Love waves at intermediate to  
95 long periods with a realistic source-station distribution. Additionally, we investigate the effects of  
96 realistic noise in the data upon the inversion solutions and show to which extent they complicate  
97 comparisons between ray and finite-frequency theory.

98    **2 ASYMPTOTIC THEORY FOR MEMBRANE WAVES**

99    To obtain the asymptotic, monochromatic waveforms of membrane waves (Tanimoto 1990; Tape  
100 2003; Peter *et al.* 2007) for a laterally heterogeneous 1-D Earth, we first derive a traveling-wave  
101 expression of membrane waves for a homogeneous model. To then account for lateral hetero-  
102 geneities, we calculate the phase and amplitude anomalies for a laterally heterogeneous phase-

velocity distribution by a ray-tracing algorithm. We use them to correct the homogeneous wave-forms.

## 2.1 From standing waves to traveling waves

The idea is to start from a standing-wave representation of membrane waves and derive an analytical, asymptotic formulation in terms of traveling waves. Following the work of Gilbert (1976), we will conduct here a simplified treatment for waves propagating on a zero-thickness, spherical membrane (Tanimoto 1990). Motion on a membrane with wave velocity  $c$  is described by the equation

$$\left[ \frac{1}{c^2(\theta, \phi)} \partial_t^2 - \nabla_1^2 \right] u(\theta, \phi, t) = f(\theta, \phi, t) \quad (1)$$

(e.g., Peter *et al.* 2007), where the displacement  $u(\theta, \phi, t)$  depends on colatitude  $\theta$ , longitude  $\phi$  and time  $t$ , while  $\partial_t$  and  $\nabla_1^2$  denote time derivation and surface Laplacian on the sphere respectively.

We prescribe a forcing term

$$f(\theta, \phi, t) = \frac{e^{-\Delta^2/2\mu^2}}{\mu^2} \cdot \frac{-t e^{-t^2/2\sigma^2}}{\sigma^2 \sqrt{2\pi}\sigma}, \quad (2)$$

with arc-distance from the source  $\Delta \in [0, \pi]$ . The source parameters  $\sigma$  and  $\mu$  govern the characteristic frequency content of the source. An analytical solution  $u(\theta, \phi, t)$  is available for a constant velocity  $c_0$  (Tape 2003, eq. 3.34):

$$u(\theta, \phi, t) = c_0^2 \sum_{l=0}^{\infty} \left( l + \frac{1}{2} \right) I_l(\mu) \cos(\omega_l t) e^{-\omega_l^2 \frac{\sigma^2}{2}} P_l(\cos \theta), \quad (3)$$

with  $P_l$  denoting the Legendre polynomials of degree  $l$ . The angular frequency  $\omega_l$  at degrees  $l = 0, 1, 2, \dots$  is given by

$$\omega_l = \frac{c_0 \sqrt{l(l+1)}}{a} \quad (4)$$

for a given surface radius  $a$ . The integrals

$$I_l(\mu) = \int_0^\pi P_l(\cos(\alpha)) \frac{e^{-\frac{\alpha^2}{2\mu^2}}}{\mu^2} \sin(\alpha) d\alpha \quad (5)$$

can be evaluated numerically. Note that the waveform  $u(\theta, \phi, t)$  due to this initial source and given by eq. (3) is represented as a standing-wave summation.

## 6 Peter et al.

### 2.1.1 Asymptotic approach and orbit separation

We rewrite eq. (3) with an asymptotic expression for the Legendre polynomials  $P_l$  (Gilbert 1976, eq. 9), valid for large degrees  $l$ . Additionally, we substitute  $\lambda = l + \frac{1}{2}$  and separate even from odd orbits, following the derivation of Ferreira (2005, Appendix B.1). Hence, we can rewrite

$$u(\theta, \phi, t) = \sum_{\lambda=\frac{1}{2}, \frac{3}{2}, \dots}^{\infty} [f_+(\lambda)e^{i\lambda\theta} + f_-(\lambda)e^{-i\lambda\theta}] \cos(\omega_\lambda t), \quad (6)$$

where

$$f_+(\lambda) = \frac{1}{2} c_0^2 \lambda I_\lambda(\mu) \left\{ \frac{2}{\pi \lambda \sin(\theta)} \right\}^{\frac{1}{2}} e^{-\omega_\lambda^2 \frac{\alpha^2}{2}} e^{-i\frac{\pi}{4}}, \quad (7)$$

$$f_-(\lambda) = f_+^*(\lambda), \quad (8)$$

with  $*$  denoting a complex conjugate. The coefficients  $f_+$  belong to waves for even orbits while the coefficients  $f_-$  to those for odd orbits. From the standing-wave solution (6), applying Poisson's formula and transforming to frequency domain, we find the expression

$$u(\theta, \phi, \omega) = \sum_{s=-\infty}^{\infty} (-1)^s \int_0^\infty [f_+(\lambda)e^{-i\lambda(2\pi s - \theta)} + f_-(\lambda)e^{-i\lambda(2\pi s + \theta)}] \frac{\omega}{i(\omega^2 - \omega_\lambda^2)} d\lambda, \quad (9)$$

which has single poles at  $\omega = \pm\omega_\lambda$ . Taking advantage of the general dispersion relation  $\omega(\lambda)$ , which for the membrane wave model becomes

$$\omega_\lambda \approx \frac{c_0 \lambda}{a}, \quad (10)$$

we apply Cauchy's residue theorem to obtain

$$u(\theta, \phi, \omega) \approx \sum_{s=-\infty}^{\infty} (-1)^s [f_+(\lambda(\omega))e^{-i\lambda(\omega)(2\pi s - \theta)} + f_-(\lambda(\omega))e^{-i\lambda(\omega)(2\pi s + \theta)}] \frac{2\pi a}{c_0}, \quad (11)$$

where terms  $f_\pm(-\lambda(\omega))$  are ignored. Finally, eq. (11) is Fourier-transformed back to time domain to find the traveling-wave solution

$$u(\theta, \phi, t) \approx \frac{1}{2\pi} \int_{-\infty}^{\infty} \sum_{s=-\infty}^{\infty} (-1)^s [f_+(\lambda(\omega))e^{-i\lambda(\omega)(2\pi s - \theta)} + f_-(\lambda(\omega))e^{-i\lambda(\omega)(2\pi s + \theta)}] \frac{2\pi a}{c_0} e^{i\omega t} d\omega. \quad (12)$$

## 2.2 Traveling waves on a homogeneous membrane

The traveling-wave solutions for different orbits follow from the expression (12). For example, for odd orbits we set  $f_+(\lambda(\omega)) \equiv 0$  and use  $s = 0, 1, 2, \dots$  for the first, third, fifth and so on orbit. The

148 corresponding expressions for the first and third orbits are

$$\text{R1: } u(\theta, \phi, t) \approx \frac{a}{c_0} \int_{-\infty}^{\infty} f_-(\lambda(\omega)) e^{-i\lambda(\omega)\theta} e^{i\omega t} d\omega \quad (13)$$

$$\text{R3: } u(\theta, \phi, t) \approx -\frac{a}{c_0} \int_{-\infty}^{\infty} f_-(\lambda(\omega)) e^{-i\lambda(\omega)(2\pi+\theta)} e^{i\omega t} d\omega. \quad (14)$$

149 For even orbits, we set  $f_-(\lambda(\omega)) \equiv 0$  and use  $s = 1, 2, 3, \dots$  for the second, forth, sixth and so on  
150 orbit. The following expressions are for the second and forth orbits:

$$\text{R2: } u(\theta, \phi, t) \approx -\frac{a}{c_0} \int_{-\infty}^{\infty} f_+(\lambda(\omega)) e^{-i\lambda(\omega)(2\pi-\theta)} e^{i\omega t} d\omega \quad (15)$$

$$\text{R4: } u(\theta, \phi, t) \approx \frac{a}{c_0} \int_{-\infty}^{\infty} f_+(\lambda(\omega)) e^{-i\lambda(\omega)(4\pi-\theta)} e^{i\omega t} d\omega. \quad (16)$$

151 In order to plot the corresponding waveform solutions, we calculate the integrands of eqs. (13)  
152 through (16) at each  $\omega$  explicitly, and use a numerical integration to find  $u(\theta, \phi, t)$ . The Legendre  
153 polynomials  $P_l$  for non-integer values of the angular degree  $l(\omega) = \lambda(\omega) - \frac{1}{2}$ , with  $\lambda(\omega) =$   
154  $\sqrt{\frac{\omega^2 a^2}{c_0^2} + \frac{1}{4}}$ , are found numerically by spline interpolation. Similarly, the integrals  $I_l(\mu)$ , given by  
155 eq. (5), were interpolated by splines for non-integer values of the angular degree  $l(\omega)$ .

### 156 2.2.1 Waveform example

157 We choose an initial source-station pair with epicentral distance of about  $90^\circ$  and compare the  
158 asymptotic solution against the numerical one. Figure 1 shows the waveform for the fourth orbit  
159 obtained by the asymptotic approach of eq. (16) together with the numerical solution, calculated by  
160 finite-differences integration on a spherical membrane (Peter *et al.*, 2007). Note that the numerical  
161 solution provides all orbits up to the end time of the computation. The asymptotic waveform has  
162 a slightly smaller amplitude at maximum displacement than the numerical one. The phase offset  
163 between the two is small. The agreement in this homogeneous case is good enough to proceed and  
164 obtain an asymptotic trace for a laterally heterogeneous model.

## 165 2.3 Ray theory on a heterogeneous membrane

166 The asymptotic approach provides us with a waveform for a homogeneous membrane-wave model.  
167 To extend the treatment of section 2.2 to the heterogeneous case, we first use the laws of optics

<sup>168</sup> to determine the ray path travelled by a wave (Woodhouse & Wong 1986; Boschi & Woodhouse  
<sup>169</sup> 2006), then compute the phase by integration along such a ray.

<sup>170</sup> 2.3.1 *Ray-tracing*

<sup>171</sup> In order to calculate the phase  $\psi_{het}$  for a heterogeneous background model

$$\psi_{het} = \int_{ray} \frac{\omega}{c(\theta, \phi)} ds \quad (17)$$

<sup>173</sup> with local phase velocities  $c(\theta, \phi)$ , we need to compute the corresponding ray between the seismic  
<sup>174</sup> source and a receiver station, a problem treated by Woodhouse & Wong (1986) for the sphere. For  
<sup>175</sup> brevity, we just give the two equations which relate to our case here. We simultaneously solve for

<sup>176</sup>  $\gamma(\phi) \equiv \cot \theta$  and  $\gamma'(\phi) = \frac{d\gamma}{d\phi}(\phi)$  in equations (33) and (38) of Woodhouse & Wong (1986):

$$\frac{d^2\gamma}{d\phi^2} + \gamma = \left( \frac{\nu^2}{1 + \gamma^2} \right) (\partial_\theta - \nu \partial_\phi) \ln c(\theta, \phi) \quad (18)$$

$$\begin{aligned} \frac{d^2\gamma'}{d\phi^2} + \gamma' &= \frac{2\nu}{1 + \gamma^2} \left( \nu' - \frac{\nu\gamma\gamma'}{1 + \gamma^2} \right) (\partial_\theta - \nu \partial_\phi) \ln c(\theta, \phi) \\ &\quad - \left( \frac{\nu^2}{1 + \gamma^2} + 1 \right) \frac{\gamma'}{1 + \gamma^2} (\partial_\theta^2 - \nu \partial_\theta \partial_\phi) \ln c(\theta, \phi) \\ &\quad - \left( \frac{\nu^2}{1 + \gamma^2} + 1 \right) \nu' \partial_\phi \ln c(\theta, \phi) \end{aligned} \quad (19)$$

<sup>177</sup> where  $\nu(\phi) \equiv -\gamma'(\phi) = -\frac{d\gamma}{d\phi}(\phi)$  and ' denotes differentiation with respect to the initial value of  
<sup>178</sup>  $\nu$ , at constant  $\phi$ . The boundary conditions are  $\gamma'(0) = 0$  and  $\nu'(0) = 1$ .

<sup>179</sup> 2.3.2 *Ray-theoretical travel-time anomalies*

<sup>180</sup> Let us rotate the reference frame such that source and receiver are located on the equator.  $\phi_k$   
<sup>181</sup> becomes the epicentral distance between source and receiver. For a homogeneous reference model,  
<sup>182</sup> the phase  $\psi_{hom}(\phi_k)$  can be written as

$$\psi_{hom}(\phi_k) = \int_{ray} \frac{\omega a}{c_0} d\phi = \frac{\omega a \phi_k}{c_0}, \quad (20)$$

<sup>183</sup> where  $a$  is the Earth's radius and  $c_0$  the constant phase velocity for the reference model. The phase  
<sup>184</sup> anomaly  $\delta\psi$  is defined as the difference in phase from that in the reference model, i.e. (Woodhouse  
<sup>185</sup> & Wong 1986, eq. 42)

$$\delta\psi(\phi_k) \equiv \psi_{het}(\phi_k) - \psi_{hom}(\phi_k) \quad (21)$$

$$= \frac{\omega a}{c_0} \int_0^{\phi_k} \left[ \frac{c_0}{c(\theta, \phi)} \left\{ \frac{\nu(\phi)^2}{[1 + \gamma^2(\phi)]^2} + \frac{1}{1 + \gamma^2(\phi)} \right\}^{\frac{1}{2}} - 1 \right] d\phi. \quad (22)$$

<sup>186</sup> Note that the phase anomaly  $\delta\psi$  is calculated for a single frequency  $\omega = \frac{2\pi}{\hat{T}}$  at a certain reference  
<sup>187</sup> period  $\hat{T}$ .

<sup>188</sup> We use local phase velocities  $c(\theta, \phi)$  which are derived from maps of relative phase-velocity  
<sup>189</sup> perturbations  $\frac{\delta c(\theta, \phi)}{c_0} = \frac{c(\theta, \phi) - c_0}{c_0}$  at given  $\hat{T}$  taken from Trampert & Woodhouse (1995). We can  
<sup>190</sup> define

$$\text{y}(\phi_k) = \int_0^{\phi_k} \left[ \frac{c_0}{c(\theta, \phi)} \left\{ \frac{\nu(\phi)^2}{[1 + \gamma^2(\phi)]^2} + \frac{1}{1 + \gamma^2(\phi)} \right\}^{\frac{1}{2}} - 1 \right] d\phi, \quad (23)$$

<sup>192</sup> so that

$$\frac{dy}{d\phi} = \frac{c_0}{c(\theta, \phi)} \left\{ \frac{\nu(\phi)^2}{[1 + \gamma^2(\phi)]^2} + \frac{1}{1 + \gamma^2(\phi)} \right\}^{\frac{1}{2}} - 1. \quad (24)$$

<sup>194</sup> This can be solved simultaneously with the other equations (18) and (19) from above. We pre-  
<sup>195</sup> fer working with travel-time anomalies, thus we make use of the identity between relative phase  
<sup>196</sup> anomalies and relative travel-time anomalies  $\frac{\delta\psi}{\psi_{hom}} = \frac{\delta T}{T_0}$ , where  $T_0$  denotes the travel-time for the  
<sup>197</sup> reference model. From eq. (20), we find

$$\delta\psi = \psi_{hom} \cdot \frac{\delta T}{T_0} = \frac{\omega a \phi_k}{c_0} \cdot \frac{\delta T c_0}{a \phi_k} = \omega \cdot \delta T. \quad (25)$$

### <sup>198</sup> 3 COMPARISON OF DIFFERENT APPROACHES TO THE FORWARD PROBLEM

<sup>199</sup> In order to compare predictions of travel-time anomalies, we use a setup of 38 receiver stations  
<sup>200</sup> located at about 90° epicentral distance from one source at 0° N, 0° E. The heterogeneous phase-  
<sup>201</sup> velocity model for Love waves at about 150 s period is taken from Trampert & Woodhouse (1995).  
<sup>202</sup> We conduct a series of independent experiments, where we expand the model up to degree 4, 8,  
<sup>203</sup> 12 or 20 respectively. The setup is similar to the one used in Tape (2003). For each source-station  
<sup>204</sup> pair we consider arrivals up to the fourth orbit, thus at least 152 prediction values are compared for  
<sup>205</sup> each of the four different models. The numerically derived values, which are recalculated for each  
<sup>206</sup> model with different degree of complexity, can be seen as the “true” values, which the predicted  
<sup>207</sup> ones should match in an ideal case.

208 **3.1 Evaluation of ray theory**

209 We first compare the ray-theoretical predictions of travel-time anomalies against numerically cal-  
 210 culated travel-time anomalies. A reference trace for the homogeneous model and a second trace  
 211 for the heterogeneous model are computed numerically with the finite-differences approach of Pe-  
 212 ter *et al.* (2007). We bandpass-filter the two numerical traces around an angular frequency  $\omega$ , for  
 213 which we have also determined ray-theoretical travel-time anomalies  $\delta T$  according to eq. (25).  
 214 The bandpass-filter uses a half-bandwidth of 2.5 mHz around the center frequency  $\omega$ . Following  
 215 Ekström *et al.* (1997), we then determine the corresponding numerical travel-time anomaly by a  
 216 nonlinear downhill-simplex algorithm (Nelder & Mead 1965). We checked this algorithm against  
 217 a cross-correlation measurement technique and found almost identical results for the phase anom-  
 218 lies.

219 Figure 2 compares the travel-time anomalies  $\delta T$  calculated by eq. (25) (RAY-exact) with the  
 220 corresponding measurements derived from the numerical simulation. Values on the diagonal cor-  
 221 respond to perfect agreement. We see that ray theory predicts the first-orbit anomalies accurately;  
 222 for higher orbits (shown with different symbols), the values are more scattered around the diag-  
 223 onal, particularly for models with energy at increasingly high harmonic degrees (compare Figure  
 224 2a with 2b, 2c and 2d). In general, the plots of Figure 2 are in agreement with the results of Tape  
 225 (2003). Particularly large differences between the ray-theoretical prediction and the ground-truth  
 226 value for higher orbits and expansions are observed when multiple ray paths between source and  
 227 receiver location exist (in such cases, we plot in Figure 2 the phase-anomaly associated with the  
 228 first ray found by our ray-tracing algorithm).

229 In general, Figure 2 confirms two aspects of ray theory: first, ray-theoretical predictions are  
 230 closely related to the ratio between the scalelength  $\Lambda$  of heterogeneities and the wavelength  $\lambda$   
 231 under consideration. Predictions are valid when  $\lambda \ll \Lambda$ , and the fit systematically decreases as the  
 232 maximum harmonic degree of heterogeneity grows, from Figure 2a to 2d. Secondly, we see that  
 233 ray-theoretical predictions depend on the travelled epicentral distance between source and receiver  
 234 location. The longer the travelled distance (the higher the orbit), the less accurate ray-theoretical  
 235 predictions become.

236 **3.2 Evaluation of finite-frequency theory**

237 We also consider the travel-time anomalies  $\delta T$  predicted on the basis of the finite-frequency ker-  
 238 nels derived by the single scattering approximation, specifically the numerical kernels  $K_{num}(\theta, \phi)$   
 239 from Peter *et al.* (2007). These kernels were derived by the adjoint method (Tromp *et al.* 2005  
 240 and references therein) and computed for the homogeneous background model. We calculate the  
 241 corresponding travel-time anomaly  $\delta T$  by integrating

$$242 \frac{\delta T}{T_0} = \int_{\Omega} K_{num}(\theta, \phi) \frac{\delta v}{v_0} d\Omega \quad (26)$$

243 over the surface  $\Omega$  of the membrane, and multiplying with the reference travel time  $T_0$  of the  
 244 homogeneous case.  $\frac{\delta v}{v_0}$  denotes relative phase-velocity perturbations in the model of Trampert &  
 245 Woodhouse (1995) expanded up to degree 4, 8, 12 or 20. Figure 3 compares the travel-time anom-  
 246 alies  $\delta T$  calculated this way, with the corresponding ground-truth ones. The kernels  $K_{num}(\theta, \phi)$  are  
 247 computed for every orbit separately. An example of the numerical kernels for a particular source-  
 248 station pair for all four orbits is given in Figure 4. Note that the shape of the kernels is strongly  
 249 affected by the filtering at 150 s period (corresponding to the measurement technique) with a  
 250 half-bandwidth of 2.5 mHz.

251 Analyzing the scatter in Figures 2 and 3, we find that finite-frequency predictions for the first  
 252 orbit are more accurate than the ray-theoretical ones of Figure 2. As a quantitative measure of  
 253 scatter, we used a linear regression to calculate the RMS of the residuals, which for ray-theoretical  
 254 predictions of first orbit arrivals range between 0.06–1.36 s for the background phase-velocity map  
 255 filtered to degree 4, 8, 12 and 20 (Figures 2a to 2d). The corresponding RMS range for residuals of  
 256 the finite-frequency predictions of first orbit arrivals shown in Figure 3a to 3d are between 0.05 –  
 257 0.57 s. At higher orbits, the situation is reversed, with ray theory predicting ground-truth travel-  
 258 time anomalies more accurately than the finite-frequency kernels. We tested these numerical kernel  
 259 predictions also against predictions from analytical kernels for the first and second orbit, calculated  
 260 as in Spetzler *et al.* (2002). The scatterplot results shown in Figure 5a to 5d are analogous to  
 261 those found from numerical kernels. The RMS of the residuals of the (analytical) finite-frequency  
 262 predictions range for the first orbit between 0.08 – 0.68 s. For second orbit arrivals, they range

263 between  $0.79 - 8.83$  s, compared to  $0.92 - 8.40$  s for the predictions based on numerical sensitivity  
 264 kernels and  $0.19 - 6.99$  s for the ray-theoretical ones. A similar effect has been noted in attempts  
 265 to compute higher-orbit travel times by the integration of fully 3-D surface wave kernels (personal  
 266 communication with Y. Capdeville).

267 The accuracy of prediction depends upon the ratio of the scalelength  $\Lambda$  of heterogeneities to  
 268 the width  $W$  of the first Fresnel zone. Baig *et al.* (2003) and Dahlen (2004) define a dimensionless  
 269 “doughnut-hole” parameter  $D$  valid for their 3-D sensitivity kernels in a cartesian box model

$$270 \quad D^{3D} = \frac{\Lambda}{W} = \frac{\Lambda}{\sqrt{\lambda \cdot L}} \text{ (3-D cartesian)}, \quad (27)$$

271 where  $L$  denotes the travelled distance and  $\lambda$  the wavelength. Spetzler & Snieder (2001) adapted  
 272 the width  $W = \sqrt{\frac{3}{2}\lambda \tan(\frac{L}{2})}$  to spherical geometry, limited to the 2-D (surface-wave phase veloc-  
 273 ity) case, thus

$$274 \quad D^{2D} = \frac{\Lambda}{W} = \frac{\Lambda}{\sqrt{\frac{3}{2}\lambda \tan(\frac{L}{2})}} \text{ (sphere)}. \quad (28)$$

275 In general, it is assumed that for  $D \rightarrow \infty$ , ray-theoretical predictions would become perfectly  
 276 accurate.

277 For wave propagation in a weakly heterogeneous, 3-D cartesian box, Baig *et al.* (2003) found  
 278 that finite-frequency predictions are accurate for  $D^{3D} \geq 0.1$ , and ray-theoretical ones only for  
 279  $D^{3D} \geq 0.5$ . Yang & Hung (2005) found that for analytical finite-frequency sensitivity kernels, in  
 280 a similar 3-D case, travel-time predictions are only accurate for weakly heterogeneous media with  
 281 perturbations  $\leq 3\%$ . Their fig. 2 shows that “Born” theory predictions are less accurate than those  
 282 of exact (general) ray theory for  $1.1 \leq D^{3D} \leq 1.5$ . In our heterogeneous models, phase-velocity  
 283 perturbations can amount to about  $\pm 6\%$ , and depending upon the maximum degree of harmonic  
 284 expansion,  $\Lambda$  varies between  $1,953 - 8,896 \text{ km}$ , with corresponding doughnut-hole parameters  
 285  $0.7 \leq D^{2D} \leq 3.4$  (for our first orbit kernels with  $90^\circ$  epicentral distances). In this scenario, we  
 286 find finite-frequency kernels to perform better than ray theory as a solution to the forward problem.

287 **3.3 Multiple ray-path example**

288 Ray-theoretical predictions are especially inaccurate in cases where multiple rays are found (Tape  
289 2003). A reference case is chosen here for a source-station pair such that we obtain three ray paths,  
290 for the fourth orbit, which arrive at the same station location (source at equator 0° N / 0° W, station  
291 at about 25° N / 90° W). Rays are traced, and phase calculated in the 150 s Love wave phase-  
292 velocity map of Trampert & Woodhouse (1995), with a spherical harmonics expansion up to degree  
293 10. The considered case is the only multi-pathing occurrence found for this phase-velocity map and  
294 maximum harmonic degree, among 38 investigated source-station pairs with about 90° epicentral  
295 distance. If the model is filtered to lower harmonic degree, no multiple ray paths are found for  
296 the same source-station pairs; at higher harmonic degrees, multi-pathing becomes increasingly  
297 frequent.

298 The ray-tracing algorithm calculates for each ray, denoted by  $i = 1, 2, 3$ , the corresponding  
299 phase anomaly  $\delta\psi_i$ , which is further divided by the angular frequency to obtain the correspond-  
300 ing travel-time anomaly  $\delta T_i$  for monochromatic waves with a period of about 150 s. To obtain  
301 the waveform, the amplitude anomaly for each ray is considered as well. The cumulative trav-  
302 elled epicentral distance from source to receiver is 630°. The ray-theoretical predicted values are  
303 applied to the monochromatic trace  $\tilde{u}(\theta, \phi, t)$  obtained by filtering first the asymptotic waveform  
304 for the fourth orbit (see section 2.2). We further corrected the travel-time and amplitude of the  
305 monochromatic waveform for all three rays separately by the predicted travel-time anomaly  $\delta T_i$   
306 and amplitude anomaly  $A_i$  to obtain three single waveforms

307 
$$\tilde{u}_i(\theta, \phi, t) = A_i \cdot \tilde{u}(\theta, \phi, t + \delta T_i). \quad (29)$$

308 Finally, all three waveforms are summed up to obtain the resulting one

309 
$$\tilde{u}_{res}(\theta, \phi, t) = \sum_i \tilde{u}_i(\theta, \phi, t). \quad (30)$$

310 Note that  $\tilde{u}_{res}(\theta, \phi, t)$  is now valid for the heterogeneous model.

311 Eq. (30) is also implemented via the harmonic addition theorem, expressing the sum of  $n$   
312 harmonic waves as

$$313 \quad \sum_{i=1}^n A_i \cos(\omega t + \delta\psi_i) = A \cos(\omega t + \delta\psi), \quad (31)$$

314 where

$$A^2 \equiv \sum_{i=1}^n \sum_{j=1}^n A_i A_j \cos(\delta\psi_i - \delta\psi_j), \quad (32)$$

$$\tan(\delta\psi) = \frac{\sum_{i=1}^n A_i \sin(\delta\psi_i)}{\sum_{i=1}^n A_i \cos(\delta\psi_i)}. \quad (33)$$

315 Hence, the resulting phase anomaly  $\delta\psi$ , resp. travel-time anomaly  $\delta T$ , and amplitude anomaly  $A$   
 316 of  $\tilde{u}_{res}(\theta, \phi, t)$  as defined by eq. (30) can be calculated directly from the single predictions  $\delta\psi_i$  and  
 317  $A_i$ . We compare all values with the travel-time and amplitude anomaly obtained by the numerical  
 318 algorithm in Table 1.

319 We observed that the resulting, asymptotic waveform, given by eq. (30), was shifted by about  
 320 17 seconds and exhibited a slightly larger amplitude of about 5% with respect to the numeri-  
 321 cal, ground-truth trace. Note that the discrepancy of these observed anomalies to the analyti-  
 322 cal, harmonic values from Table 1 might be found in the finite bandwidth of the single traces  
 323  $\tilde{u}_i(\theta, \phi, t)$  used for the summed waveforms of eq. (30), while the analytical values are valid only  
 324 for monochromatic waves. Still, the travel-time anomaly of the resulting trace  $\tilde{u}_{res}(\theta, \phi, t)$  is closer  
 325 to the numerical, ground-truth prediction than the single predictions for the second and third ray,  
 326 but worse than the prediction of the first ray. It is therefore crucial to find all rays in order to  
 327 properly account for the predicted anomalies.

328 Our study differs with respect to the work on synthetic seismograms of a more realistic case  
 329 by Wang & Dahlen (1994, see fig. 21). We consider only the monochromatic (or very narrowly  
 330 filtered) waveform for an analytical source, instead of an integration over a complete frequency  
 331 range. Such an integration becomes more expensive as for each frequency the corresponding,  
 332 ray-theoretical phase and amplitude anomalies must be found first. Additionally, we investigated  
 333 especially a multiple ray-path example where Wang & Dahlen (1994) only consider single ray  
 334 examples. A more systematic investigation of multi-pathing effects as done here could in principle  
 335 be conducted with the membrane-wave model (Tanimoto 1990; Tape 2003; Peter *et al.* 2007).

336 **4 COMPARISON OF DIFFERENT APPROACHES TO THE INVERSE PROBLEM**

337 To compare the performance of different tomographic methods in different scenarios, we construct  
 338 a number of independent databases of ground-truth, numerically computed phase anomalies of 150  
 339 s Love waves, and invert them either by a ray-theoretical or a finite-frequency algorithm. Differ-  
 340 ences in the solution maps can then be ascribed to the effects of different theoretical descriptions  
 341 of seismic wave propagation. Databases are derived from three “checkerboard” phase-velocity  
 342 maps of different spatial frequency, as well as from the model of Trampert & Woodhouse (1996).  
 343 We also experiment with the amplitude of “input” anomalies, and with the realistic random noise  
 344 added to the synthetics. We invert each ground-truth dataset on a grid of approximately equal-area  
 345 pixels, of extent  $3^\circ \times 3^\circ$  at the equator. Linearized ray-theory and numerical sensitivity kernels  
 346 (Peter *et al.*, 2007) are used independently to construct the corresponding matrices relating the  
 347 phase-velocity perturbations to the data.

348 In both cases, an iterative least-squares algorithm (Paige & Saunders 1982; implemented as  
 349 in Boschi 2006) finds the phase-velocity solution to the inverse problem, with only roughness-  
 350 damping and no norm-damping applied. We repeat the inversions with different roughness-damping  
 351 coefficients (Boschi 2006; Boschi *et al.* 2006; Peter *et al.* 2007) and visualize the “L-curves”,  
 352 where the misfit to the data is plotted versus the normalized model roughness (as defined by Boschi  
 353 2006). Collocating the resulting inversion maps for different damping values, we also form anima-  
 354 tions illustrating the dependence of solutions on the regularization scheme (<http://www.seg2.ethz.ch/dpeter/inversions.html>). As explained by Boschi (2006) in his section 4 and fig. 3, if different for-  
 355 mulations of the inverse problem are applied, equal numerical values of the damping parameter  
 356 do not lead to equally regularized solutions from the different approaches; to identify equivalently  
 357 regularized solutions from ray-theory and finite-frequency inversions, we use here the criterion of  
 358 equal curvature on the respective L-curves (Peter *et al.* 2007). In the following, we compare such  
 359 preferred inversion solutions found from ray theory versus finite-frequency theory.

361 **4.1 Data coverage**

362 We employ the same source-station pairs as in the database of Ekström *et al.* (1997), updated  
 363 as described by Boschi & Ekström (2002), for minor-arc Love waves at 150 s period. For each  
 364 source-station pair, we construct a synthetic measurement by cross-correlation between the trace  
 365 obtained for a homogeneous background model, and the trace calculated for a corresponding later-  
 366 ally heterogeneous input model. The number of synthetic measurements ( $\sim 10^4$ ) is therefore equal  
 367 to the number of observations in the real dataset at this period. Figure 7 shows the great-circle rays  
 368 for all measurements with the chosen source-station distribution. The data coverage defined by the  
 369 number of rays passing through each single pixel of the inversion grid coincides with that of Peter  
 370 *et al.* (2007, fig. 12). Regions with the highest number of ray-counts are distributed over Asia and  
 371 North America. The Southern Hemisphere in general has relatively poor data coverage.

372 **4.2 Scalelength test**

373 We compare the inversions of synthetic data computed in single-harmonic “checkerboard” models  
 374 of different spatial frequency (degrees). Ray theory is a high-frequency approximation. In practice,  
 375 this leads to the condition that the wavelength under consideration should be small compared to the  
 376 scalelength of heterogeneities it travels through. In order to illustrate the effect of this assumption  
 377 upon the performance of the inverse method, we can either (i) change the size of the perturbations  
 378 in the input models or (ii) consider smaller wavelengths/wave periods.

379 Figure 8 and Figure 9 show the results of experiment (i) and (ii) respectively. For Figure 8  
 380 of experiment (i), the synthetic datasets for each input model used Love waves at 150 s period  
 381 to obtain the waveform for the homogeneous and heterogeneous case. Ray-theoretically derived  
 382 solutions start differing from finite-frequency solutions for the higher degree input models. The  
 383 lengthscale of the perturbations for the chosen input models vary in a range of  $\sim 2,000 - 4,000$   
 384 km, i.e. about three to six times the wavelength under consideration. Figure 9 follows the idea (ii)  
 385 and changes the wave period down to 100 s in order to derive the synthetic datasets for the two  
 386 higher degree checkerboards of the previous example. In this case, at the highest degree model, the

lengthscale of perturbations is about four times the wavelength. Especially for regions with good data coverage, the inversions can retrieve the input model fairly accurately.

From a comparison of Figure 8a with 8b or 8c, or of Figure 9a with 9b, we infer that finite-frequency methods, applied to minor-arc phase-velocity data at the periods under consideration, perform significantly better at smaller scalelengths of heterogeneity than ray-theoretical methods. Differences between ray-theoretical and finite-frequency solutions are small for low-degree “input” models ( $< 10$ : Figure 8a), but start to become significant for higher degrees ( $\geq 13$ : Figure 8b, 8c, 9b). Considering shorter wavelengths, this effect shifts to higher spherical harmonic degrees (compare Figure 8b with 9a). The finite-frequency solutions clearly retrieve the input structures with higher accuracy. Differences are most prominent in regions with lower data coverage (oceans, Southern Hemisphere), where ray theory is systematically less accurate. As a general rule, in this ideal case without any noise in the data, finite-frequency solutions achieve a much better datafit than ray-theoretical ones.

### 4.3 Noise test

The goal here is to investigate the effect of measurement errors on the tomographic images. Adding realistic noise to a synthetic database is difficult, because there can be sources of systematic errors, which are not known *a priori*, in the real databases. Ekström *et al.* (1997) estimate the quality of their observations by comparing measurements from pairs of nearby source-station pairs. In this, they are able to derive a Gaussian distribution of possible errors of the dataset. The standard deviation of this Gaussian distribution is then an estimate of the accuracy of the measurement technique. We add Gaussian random noise to the synthetic data. The standard deviation has the same size as that found by Ekström *et al.* (1997) as described above, for the same wave period. This is about 5.7 seconds in terms of travel-time shift. The error in the synthetic dataset is also checked by the same searching algorithm of pairs of source-station pairs that are within a  $3^\circ$  radius from source and receiver location.

We show in Figure 10 the results of inverting the noise-added, ground-truth database constructed from the degree 13 (Figure 10a) and degree 20 (Figure 10b) checkerboards (left panels),

414 using the ray-theory (middle panels) and finite-frequency-theory based (right panels) inverse al-  
 415 gorithms. All solutions employ a slightly higher roughness damping. In contrast to Figures 8b  
 416 and 8c, the statistical noise degrades the solutions and diminishes the differences between the two  
 417 approaches in question. This is in agreement with what suggested Sieminski *et al.* (2004). Still,  
 418 even in the presence of noise, our solutions from finite-frequency inversions are somewhat closer  
 419 to input models than those found from ray-theory ones.

420 These results are somewhat different from those obtained for global-scale inversions by Zhou  
 421 *et al.* (2005, see fig. 19). There are, however, a few important differences between their study  
 422 and ours: (i) Unlike Zhou *et al.* (2005), we construct the synthetic database by means of a non-  
 423 linearized numerical method, so that the accuracy of the synthetics is not hindered by the same  
 424 approximations used in the inversion, as is the case in classical checkerboard tests conducted by  
 425 Zhou *et al.* (2005). (ii) While Zhou *et al.* (2005) adds Gaussian-distributed, random noise with  
 426 an RMS-error of about 50% of the “structural signal”, we apply the same kind of statistical noise  
 427 but with the same standard deviation as found in the real dataset of Ekström *et al.* (1997). The  
 428 amplitude of noise is therefore different. Additionally, the effects of noise strongly depend on  
 429 the data coverage of the dataset, which is also different between the two studies. (iii) Zhou *et*  
 430 *al.* (2005) calculate analytical sensitivity kernels based upon a far-field approximation, while our  
 431 kernels are computed strictly numerically. We also use a different coarseness of the inverse grid,  
 432 which leads to different resolution of the kernels actually used by the inverse algorithm. As we use  
 433 a slightly finer parameterization, our kernels will be represented in more detail thus exhibiting a  
 434 bigger difference to rays, which itself can be assumed to lead to bigger differences in the inverse  
 435 solutions found between the two theories.

#### 436 4.4 Amplitude test

437 Both ray theory and single-scattering finite-frequency theory are linearized theories, whose per-  
 438 formance is contingent on the extent and amplitude of perturbations with respect to a reference  
 439 model, i.e. they fail when applied to (very) rough media. We next explore the specific nonlin-  
 440 ear effects of the amplitude of Earth structure heterogeneities in an example case with amplitude

441 perturbations as high as  $\pm 10\%$ . The input model pattern is a checkerboard, coinciding with the  
 442 spherical harmonic function of degree 9 and order 5 as in the previous section 4.2. The synthetic  
 443 database is then constructed for Love waves at 150 s period without any statistical noise.

444 The solution images of the inversion of the corresponding synthetic dataset are shown in Figure  
 445 11a. Comparing them with the solutions plotted in Figure 8a, we see that both theories suffer  
 446 from their inherent linearization. The power spectra of the ray-theoretical solution in Figure 11b  
 447 and of the finite-frequency solution in 11c reveal both the initial the power spectrum of the 10%  
 448 checkerboard input model with a strong peak at spherical harmonic degree 9, the finite-frequency  
 449 solution achieving a slightly higher peak. Both power spectra show further aliasing of energy  
 450 towards surrounding harmonic degrees. Note that nonlinear effects are not only degrading the  
 451 performance of both inverse methods, they also tend to affect the stability of the solutions, so that  
 452 the inversions have to be damped more strongly than in the experiments described above.

453 In order to overcome such limitations, a nonlinear solution could be found iteratively, using  
 454 the solution of a previous inversion as a new starting model to reconstruct the matrices for a new  
 455 inversion. We tested this approach in the finite-frequency case, computing all sensitivity kernels  
 456 again in the new starting model (Peter *et al.* 2007). Even after three iterations, the solution (not  
 457 shown here) did not improve significantly. Starting each iteration with a highly damped model  
 458 (and, consequently, a relatively poor datafit) increases the total number of iterations needed to find  
 459 a sufficiently good result. On the other hand, starting with a rougher model like the output models  
 460 of Figure 11, the solution is perturbed very little at each iteration. This suggests that the inverse  
 461 scheme might be trapped at a local minimum of the misfit function.

## 462 4.5 Realistic input model test

463 While the checkerboard test provides a useful measure of resolution, it is still of interest to de-  
 464 termine the way in which imperfect resolution reflects itself on the tomographic inversion of a  
 465 realistic phase-velocity distribution. We choose as input model the phase-velocity map originally  
 466 derived by Trampert & Woodhouse (1996) for Love waves at 150 s period. In comparison to our  
 467 synthetic data (section 4.1), this phase-velocity model represents a solution to a different number

468 of observations with a different source-station setup. We repeated  $\sim 10^4$  synthetic measurements  
469 (without statistical noise), based on the same source-station distribution from Ekström *et al.* (1997)  
470 as in the previous tests, to obtain the synthetic database. Figure 12a shows the preferred solutions  
471 of the ray-theoretical and finite-frequency inversion methods. The power spectra of both solutions  
472 are plotted against the power spectrum of the input model in Figure 12b and 12c; the power spec-  
473 trum of the ray-theoretical inversion result is slightly overpredicting the lowest harmonic degrees  
474 while losing energy at higher degrees ( $> 8$ ). The power spectrum of the finite-frequency solution  
475 is clearly more consistent with the input one, both at lower and at higher degrees, while the loss of  
476 resolution with increasing harmonic degree is slower than in the ray-theory case.

477 Note that both power spectra are strongly affected by the damping value chosen for the corre-  
478 sponding inversion solution. Less damping favors more energy content in the power spectrum. The  
479 strength of damping in these comparisons is therefore crucial. As ray and finite-frequency theory  
480 lead to a different sparseness and matrix representation in the inverse scheme, solution maps need  
481 different damping values that account for this fact. According to our knowledge, comparing solu-  
482 tions based on a L-curve analysis with the criterion of equal curvature values (Boschi 2006; Peter  
483 *et al.* 2007) respects such inherent smoothness. As a result, Figure 12 shows a ray-theoretical  
484 solution with a slightly larger damping coefficient than the compared finite-frequency solution.  
485 Considering such comparisons, they suggest that the finite-frequency solutions retrieve the initial  
486 power spectrum more reliably than ray-theoretical solutions.

487 In summary, our results indicate that finite-frequency inverse methods should recover the  
488 phase-velocity distribution and power spectrum of the real Earth better than ray-theory ones, par-  
489 ticularly at high harmonic degrees. Peter *et al.* (2007) inverted the phase-anomaly observations  
490 from the dataset of Ekström *et al.* (1997) for Love waves at 150 s period. Ray-theoretical and  
491 finite-frequency solutions were almost identical. In their fig. 17, the power spectrum for the finite-  
492 frequency solution reveals a slightly higher amplitude at degrees  $> 8$  as for the ray-theoretical  
493 solution. Our current results imply that this difference, although small in amplitude, reflects an  
494 improvement in the tomographic resolution of small-scale heterogeneity present in the Earth.

495 **5 CONCLUSIONS**

496 Using the asymptotic approach, we derived an analytical description of the propagation of elastic  
 497 waves on a zero-thickness membrane in terms of traveling waves, consistent with the more gen-  
 498 eral treatments of Gilbert (1976) and Ferreira (2005). We used this formulation of ray theory on a  
 499 membrane in a comparison to the forward predictions of finite-frequency kernels (analytical and  
 500 numerical: see Peter *et al.* 2007), and a ground-truth database of numerical, membrane-wave syn-  
 501 thetics. Our work extends the investigations made for 3-D sensitivity kernels within 3-D cartesian  
 502 boxes (Baig *et al.* 2003; Baig & Dahlen 2004; Dahlen 2004; Yang & Hung 2005) to a 2-D spher-  
 503 ical geometry. We further employed finite-frequency sensitivity kernels for higher orbits. While  
 504 predictions made by finite-frequency theory for first orbit arrivals are more precise than those of  
 505 ray theory, we found that finite-frequency sensitivity kernels cannot predict phase anomalies accu-  
 506 rately enough for higher orbits and even weakly heterogeneous phase-velocity models (spherical  
 507 degree expansions  $> 4$ ).

508 We also compared the tomographic inverse method based on ray theory, against the finite-  
 509 frequency tomographic algorithm of Peter *et al.* (2007), based on the adjoint method. Both ap-  
 510 proaches were applied independently to invert the same synthetic database of phase-anomaly  
 511 measurements based on a realistic source/receiver distribution (Ekström *et al.* 1997) for global  
 512 phase-velocity perturbations. The results of the latter experiment, limited to first orbit data, indi-  
 513 cate that finite-frequency theory performs significantly better than linearized ray theory. In regions  
 514 with poor data coverage, noise in the data can strongly affect the tomographic solution. This com-  
 515 plicates comparisons between ray and finite-frequency theory based on real (noisy) phase-anomaly  
 516 measurements. Nevertheless, one can expect that, in a regime of very good data coverage and qual-  
 517 ity, accounting for single scattering of intermediate- to long-period surface waves will improve  
 518 significantly the resolution of tomographic imaging.

519 **ACKNOWLEDGMENTS**

520 We thank Domenico Giardini for his constant support and Jeannot Trampert for making his phase-  
 521 velocity models available to us. Thanks also to Göran Ekström for providing his dispersion database

522 to us and Carl Tape for helpful comments. We gratefully acknowledge support from the Euro-  
 523 pean Commissions Human Resources and Mobility Programme Marie Curie Research Training  
 524 Network SPICE Contract No. MRTN-CT-2003-504267. Some figures were generated using the  
 525 generic mapping tools (GMT) (Wessel & Smith 1991).

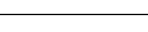
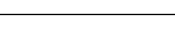
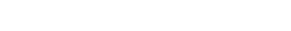
526 **REFERENCES**

- 527 Baig, A.M., F.A. Dahlen and S. H. Hung, 2003. traveltimes of waves in three-dimensional random media,  
 528 *Geophysical Journal International*, 153: p. 467-482.
- 529 Baig, A.M. and F.A. Dahlen, 2004. Statistics of traveltimes and amplitudes in random media, *Geophysical*  
 530 *Journal International*, 158: p. 187-210.
- 531 Boschi, L., 2003. Measures of resolution in global body wave tomography, *Geophysical Research Letters*,  
 532 30: p. 1978, doi:10.1029/2003GL018222.
- 533 Boschi, L., 2006. Global multiresolution models of surface wave propagation: comparing equivalently reg-  
 534 ularized Born and ray theoretical solutions, *Geophysical Journal International*, 167: p. 238-252.
- 535 Boschi, L. and G. Ekström, 2002. New images of the Earth's upper mantle from measurements of  
 536 surface wave phase velocity anomalies, *Journal of Geophysical Research-Solid Earth*, 107: p.  
 537 10.1029/2000JB000059.
- 538 Boschi, L., T. W. Becker, G. Soldati and A. M. Dziewonski, 2006. On the relevance of Born theory in global  
 539 seismic tomography, *Geophysical Research Letters*, 33: p. L06302, doi:10.1029/2005GL025063.
- 540 Boschi, L. and J.H. Woodhouse, 2006. Surface wave ray tracing and azimuthal anisotropy: a generalized  
 541 spherical harmonic approach, *Geophys. J. Int.*, , 164: p. 569-578.
- 542 Boschi, L., Ampuero, J.-P., Peter, D., Mai, P.M., Soldati, G. and D. Giardini, 2007. Petascale computing and  
 543 resolution in global seismic tomography, *Physics of the Earth and Planetary Interiors*, 163: p. 245-250.
- 544 Dahlen, F.A., S. H. Hung and G. Nolet, 2000. Frechet kernels for finite-frequency traveltimes - I. Theory,  
 545 *Geophysical Journal International*, 141: p. 157-174.
- 546 Dahlen, F.A., 2004. Resolution limit of travelttime tomography, *Geophys. J. Int.*, , 157: p. 315-331.
- 547 Ekström, G., J. Tromp and E. W. F. Larson, 1997. Measurements and global models of surface wave propa-  
 548 gation, *J. geophys. Res.*, **102**, 8137–8157.
- 549 Ferreira, A.M.G., 2005. *Seismic Surface Waves in the Laterally Heterogeneous Earth*, DPhil thesis, Univer-  
 550 sity of Oxford, U.K.
- 551 Gilbert, F., 1976. The representation of seismic displacements in terms of travelling waves, *Geophys. J. R.*  
 552 *astr. Soc.*, , 44: p. 275-280.
- 553 Laske, G., 1995. Global observation of off-great-circle propagation of long-period surface waves *Geophys.*  
 554 *J. Int.*, , 123: p. 245-259.

- 555 Laske, G. and G. Masters, 1996. Constraints on global phase velocity maps from long-period polarization  
556 data, *Journal of Geophysical Research*, 101: p. 16059-16075.
- 557 Lévêque, J. J., L. Rivera and G. Wittlinger, 1993. On the Use of the Checkerboard Test to Assess the  
558 Resolution of Tomographic Inversions, *Geophysical Journal International*, 115: p. 313-318.
- 559 Li, X. D. and T. Tanimoto, 1993. Wave-Forms of Long-Period Body Waves in a Slightly Aspherical Earth  
560 Model, *Geophysical Journal International*, 112: p. 92-102.
- 561 Li, X. D. and B. Romanowicz, 1995. Comparison of Global Wave-Form Inversions with and without Con-  
562 sidering Cross-Branch Modal Coupling, *Geophysical Journal International*, 121: p. 695-709.
- 563 Nelder, J. A. and R. Mead, 1965. A simplex-method for function minimization, *Computer Journal*, 7: p.  
564 308-313.
- 565 Paige, C.C. and M. A. Saunders, 1982. LSQR - an Algorithm for Sparse Linear-Equations and Sparse  
566 Least-Squares, *Acm Transactions on Mathematical Software*, 1: p. 43-71.
- 567 Peter, D., C. Tape, L. Boschi and J. H. Woodhouse, 2007. Surface wave tomography: global membrane  
568 waves and adjoint methods, *Geophys. J. Int.*, , 171: p. 1098-1117.
- 569 Press, W. H., S. A. Teukolsky, W. T. Vetterling and B. P. Flannery, 1992. *Numerical Recipes in FORTRAN:*  
570 *the Art of Scientific Computing*, 2nd ed. xxvi, 963, Cambridge University Press, Cambridge [England];  
571 New York, N.Y., U.S.A.
- 572 Qin, Y., Y. Capdeville, V. Maupin and J.-P. Montagner, 2006. Synthetic data set to benchmark global tomo-  
573 graphic methods, *EOS Trans AGU*, 87: p. 512.
- 574 Ritzwoller, M. H., N.M. Shapiro, M.P. Barmin and A.L. Levshin, 2002. Global surface wave diffraction  
575 tomography, *Journal of Geophysical Research*, 107: p. 2335, doi:10.1029/2002JB001777
- 576 Sieminski, A., J.J. Lévêque and E. Debayle, 2004. Can finite-frequency effects be accounted for in ray  
577 theory surface wave tomography?, *Geophys. Res. Lett.*, , 31, L24614.
- 578 Spetzler, J. and R. Snieder, 2001. The effect of small-scale heterogeneity on the arrival time of waves,  
579 *Geophysical Journal International*, 145: p. 786-796.
- 580 Spetzler, J., J. Trampert and R. Snieder, 2002. The effect of scattering in surface wave tomography, *Geo-  
581 physical Journal International*, 149: p. 755-767.
- 582 Tanimoto, T., 1990. Modeling Curved Surface-Wave Paths - Membrane-Surface Wave Synthetics, *Geophys-  
583 ical Journal International*, 102: p. 89-100.
- 584 Tape, C. H., 2003. *Waves on a Spherical Membrane*, M.Sc. thesis, University of Oxford, U.K.
- 585 Tape, C., Q. Liu and J. Tromp, 2007. Finite-frequency tomography using adjoint methods. Methodology  
586 and examples using membrane surface waves, *Geophysical Journal International*, 168: p. 1105-1129.
- 587 Trampert, J. and J. H. Woodhouse, 1995. Global phase velocity maps of Love and Rayleigh waves between  
588 40 and 150 seconds, *Geophys. J. Int.*, , 122: p. 675-690.
- 589 Trampert, J. and J. H. Woodhouse, 1996. High resolution global phase velocity distribution, *Geophys. Res.*

- 590        *Lett.*, , 23: p. 21-24.
- 591        Trampert, J. and J. H. Woodhouse, 2001. Assessment of global phase velocity models, *Geophys. J. Int.*, ,  
592                  144: p. 165-174.
- 593        Tromp, J., C. Tape and Q. Y. Liu, 2005. Seismic tomography, adjoint methods, time reversal and banana-  
594                  doughnut kernels, *Geophysical Journal International*, 160: p. 195-216.
- 595        van Heijst, H. J. and J. H. Woodhouse, 1999. Global high-resolution phase velocity distributions of overtone  
596                  and fundamental-mode surface waves determined by mode branch stripping, *Geophys. J. Int.*, 137: p.  
597                  601-620.
- 598        Wang, Z. and F. A. Dahlen, 1994. JWKB surface-wave seismograms on a laterally heterogeneous Earth,  
599                  *Geophys. J. Int.*, 119: p. 381-401.
- 600        Wessel, P. and W. H. F. Smith, 1991. Free software helps map and display data, *EOS, Transactions American*  
601                  *Geophysical Union*, 72(41): p. 441.
- 602        Woodhouse, J. H. and T. P. Girnius, 1982. Surface-Waves and Free Oscillations in a Regionalized Earth  
603                  Model, *Geophysical Journal of the Royal Astronomical Society*, 68: p. 653-673.
- 604        Woodhouse, J. H. and Y. K. Wong, 1986. Amplitude, phase and path anomalies of mantle waves, *Geophys.*  
605                  *J. R. astr. Soc.*, , 87: p. 753-773.
- 606        Yang, H. Y. and S. H. Hung, 2005. Validation of ray and wave theoretical travel times in heterogeneous  
607                  random media, *Geophysical Research Letters*, 32: p. L20302.
- 608        Yoshizawa, K. and B. L. N. Kennett, 2005. Sensitivity kernels for finite-frequency surface waves, *submitted*  
609                  to *Geophys. J. Int.*, 162: p. 910-926.
- 610        Zhou, Y., F. A. Dahlen and G. Nolet, 2004. Three-dimensional sensitivity kernels for surface wave observ-  
611                  ables, *Geophysical Journal International*, 158: p. 142-168.
- 612        Zhou, Y., F. A. Dahlen, G. Nolet and G. Laske, 2005. Finite-frequency effects in global surface-wave to-  
613                  mography, *Geophysical Journal International*, 163: p. 1087-1111.

**Table 1.** Example of multi-pathing, with three fourth-orbit rays joining source and receiver. The ground-truth value of travel-time anomaly, based on the traces computed numerically with the membrane-wave model, is compared with the ray-theoretical predictions and the resulting values by the harmonic addition theorem. Travel-times and amplitudes are based on the 150 s Love wave phase-velocity model of Trampert & Woodhouse (1995), filtered to include only harmonic degrees 10 and lower.

travel-time			amplitude		
	anomaly	[s]		anomaly	
numerical	-97.1		numerical	1.90	
ray 1	-123.6		ray 1	0.71	
ray 2	-134.4		ray 2	0.81	
ray 3	- 90.2		ray 3	1.17	
harmonic	-113.0		harmonic	1.85	

**Figure 1.** Waveform solutions on a spherical membrane by the asymptotic approach for the fourth orbit (green), or calculated numerically (red) with the finite-differences membrane-wave model of Peter *et al.* (2007).

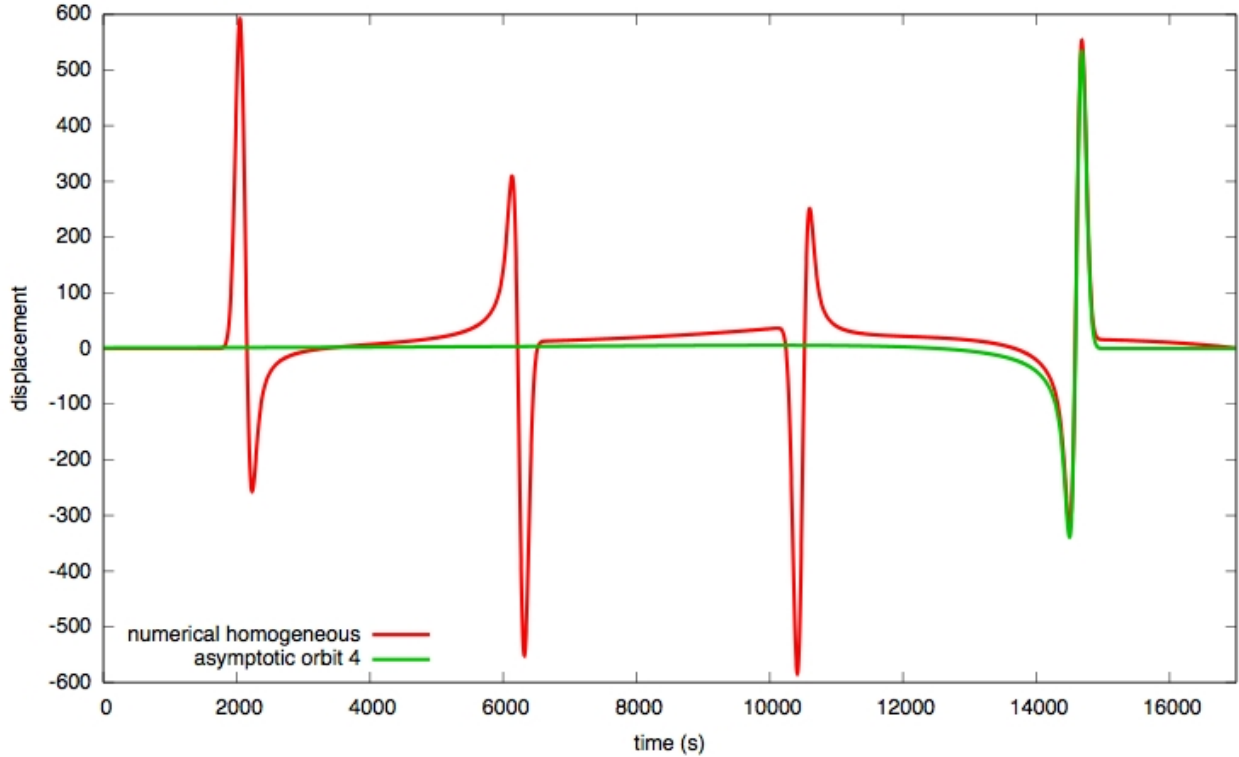
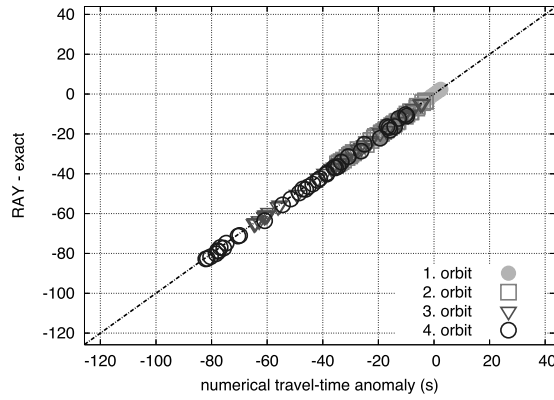
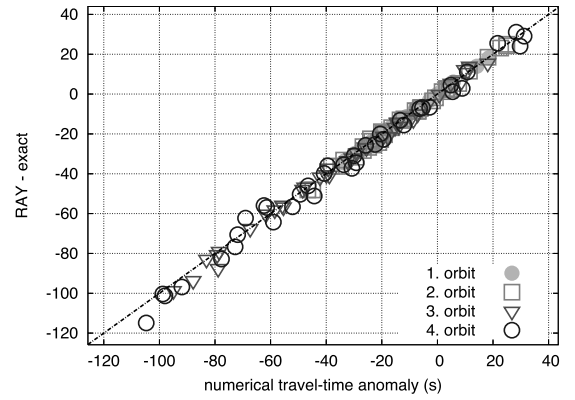


**Figure 2.** Ray-theoretical predictions of travel-time anomalies (RAY-exact) are plotted versus the numerically calculated, ground-truth ones (numerical travel-time anomaly) for 38 source-station pairs with about  $90^\circ$  epicentral distance. The source is located at  $0^\circ$  N /  $0^\circ$  E. The phase-velocity map is taken from Trampert & Woodhouse (1995) filtered to maximum harmonic degree (a) 4, (b) 8, (c) 12 and (d) 20. Predictions for the first orbit are plotted as dots (filled), second orbit as squares, third orbit as triangles and fourth orbit as circles.

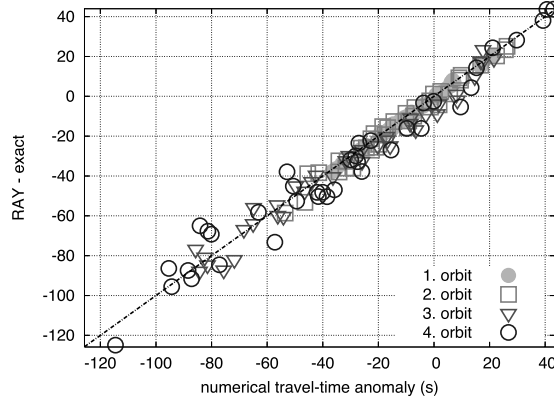
(a)



(b)



(c)



(d)

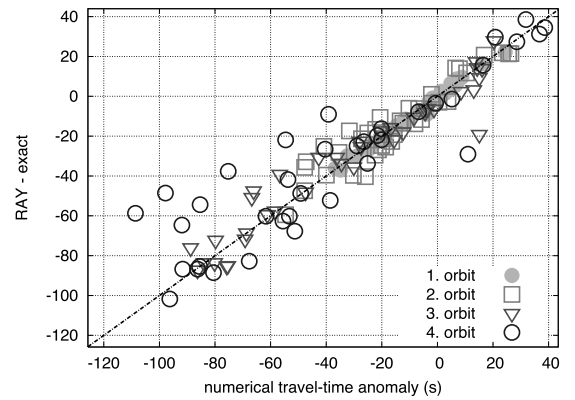
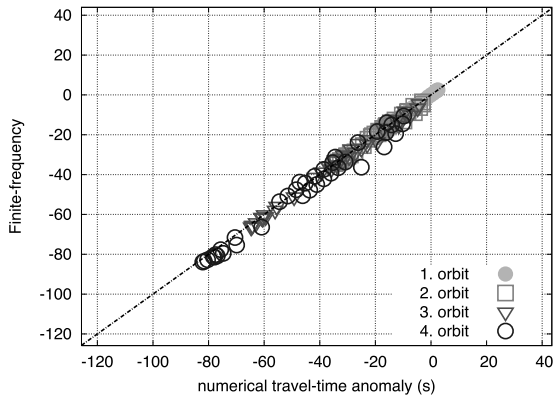
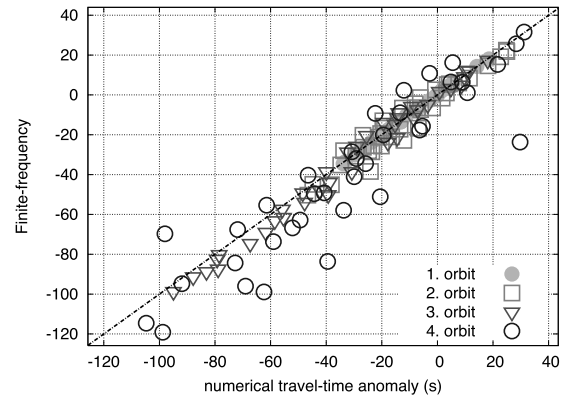


**Figure 3.** Finite-frequency predictions of travel-time anomalies (Finite-Frequency) calculated via eq. (26) are plotted versus the numerically calculated ones (numerical travel-time anomaly). Source, stations and Earth model are the same as in Figure 2. The phase-velocity map from Trampert & Woodhouse (1995) is filtered to maximum harmonic degree (a) 4, (b) 8, (c) 12 and (d) 20. Predictions for the first orbit are plotted as dots (filled), second orbit as squares, third orbit as triangles and fourth orbit as circles.

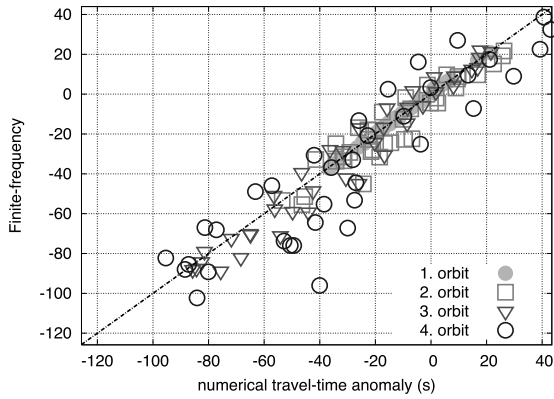
(a)



(b)



(c)



(d)

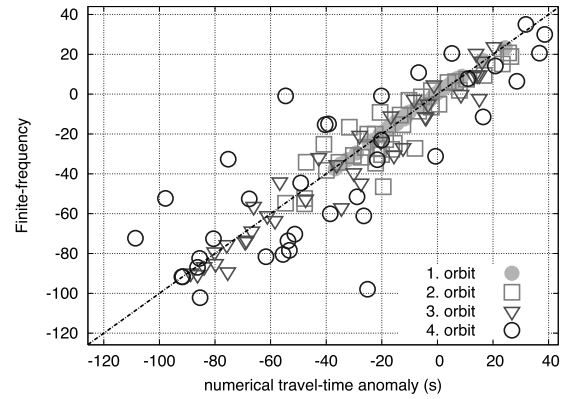


**Figure 4.** Example of numerical sensitivity kernels (Peter *et al.* 2007), based on the adjoint method, used for the predictions of travel-time anomalies (Finite-frequency) in Figure 3 for the source located at  $0^\circ$  N /  $0^\circ$  E and a receiver at  $0^\circ$  N /  $90^\circ$  E. Plotted are the relative travel-time kernels for the (a) first, (b) second, (c) third and (d) fourth orbit.

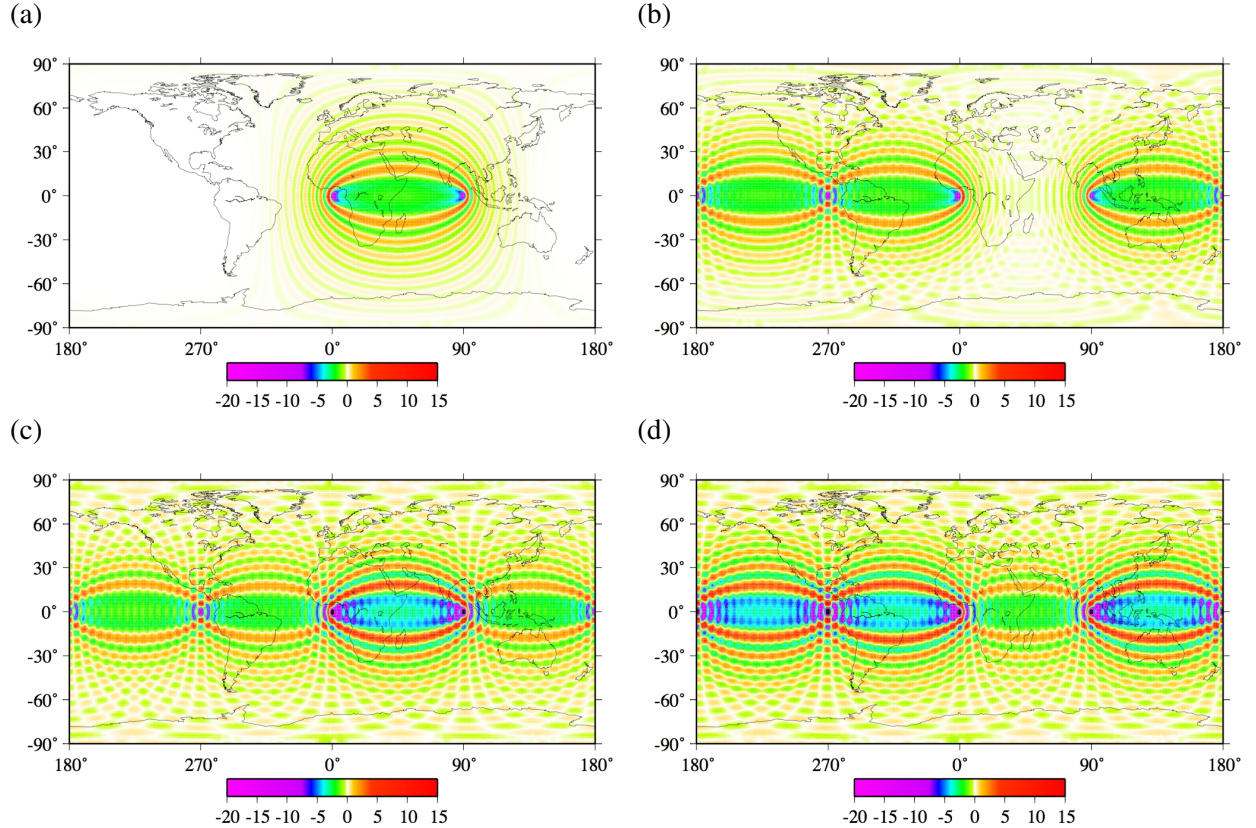


**Figure 5.** Finite-frequency predictions of travel-time anomalies using analytical sensitivity kernels for minor- and major-arcs as described by Spetzler *et al.* (2002). Source, stations and Earth model are the same as in Figure 3. The phase-velocity map from Trampert & Woodhouse (1995) is filtered to maximum harmonic degree (a) 4, (b) 8, (c) 12 and (d) 20. Predictions are shown for the first (dots, filled) and second orbit (squares). An example, similar to Figure 4, of the analytical sensitivity kernels for the source located at  $0^\circ$  N /  $0^\circ$  E and a receiver at  $0^\circ$  N /  $90^\circ$  E is given for the (e) first and (f) second orbit.

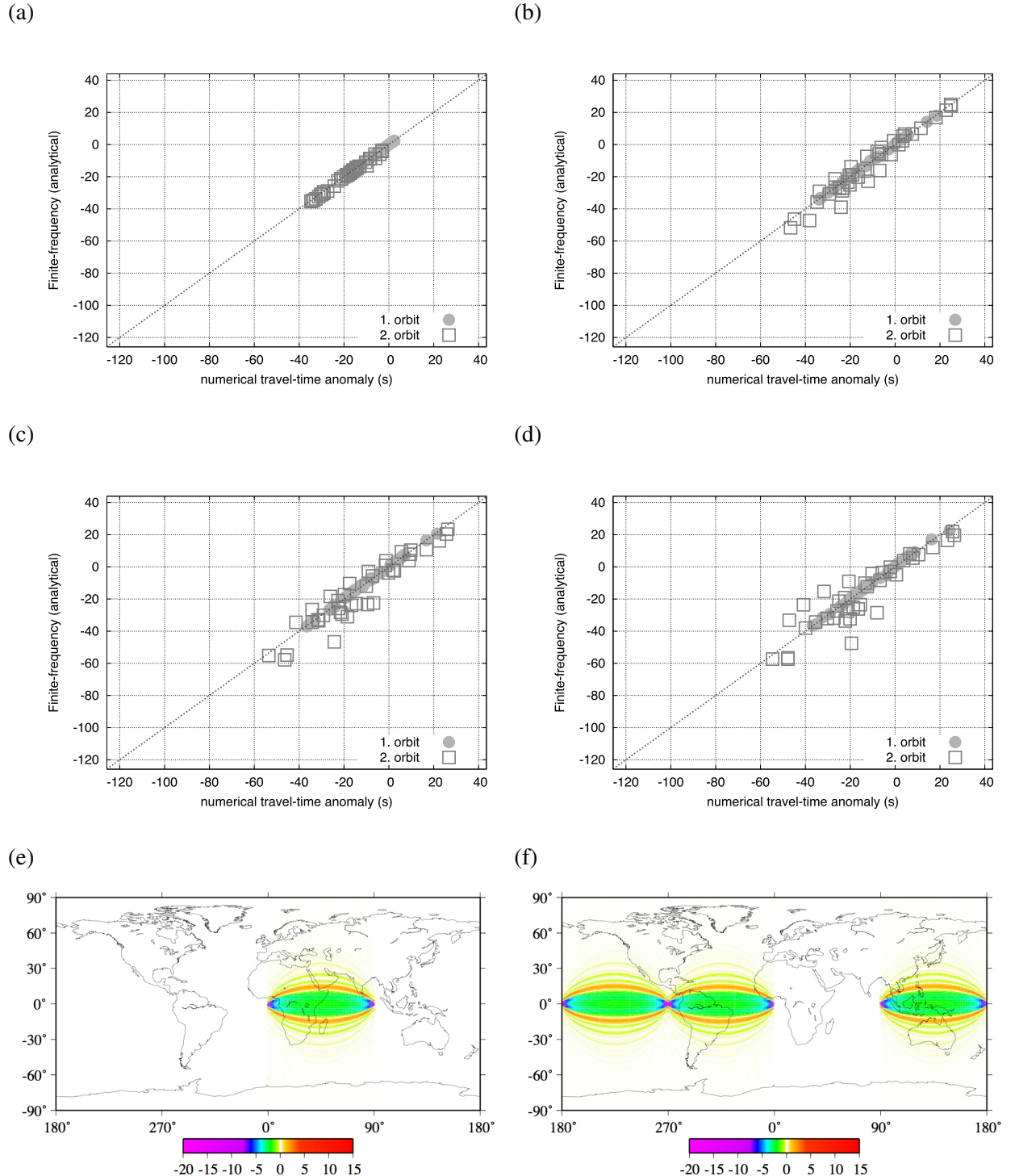


**Figure 6.** Multiple ray paths for a reference case with the fourth orbit arrival in a heterogeneous background phase-velocity distribution (Trampert & Woodhouse 1995). All three rays solve the same ray-tracing equations from Woodhouse & Wong (1986) leading to different phase- and amplitude-anomaly predictions shown in Table 1.

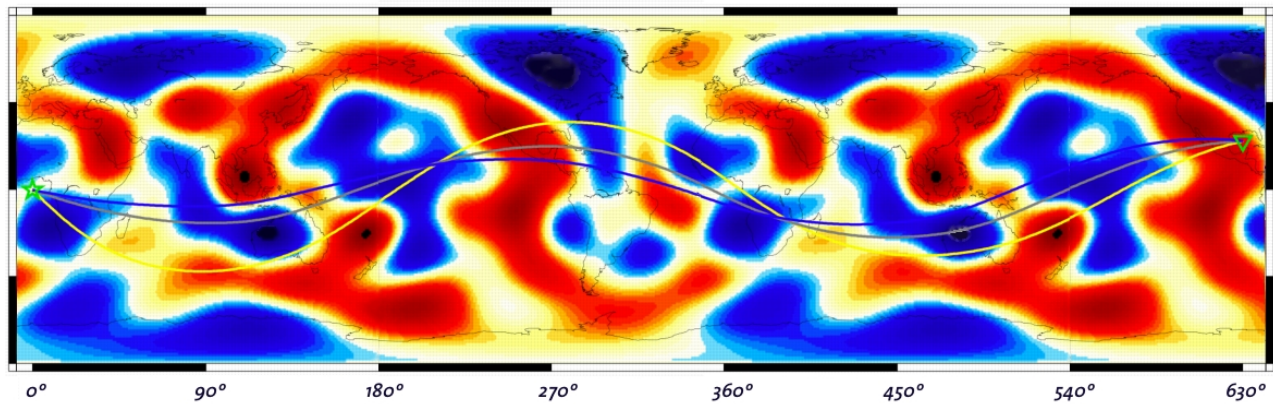


**Figure 7.** The synthetic datasets use the global distribution of sources (red stars) and stations (green triangles) taken from Ekström *et al.* (1997) for Love waves at 150 s periods. They include 16,624 measurements. For each measurement, the great-circle ray is plotted between the corresponding source and station.

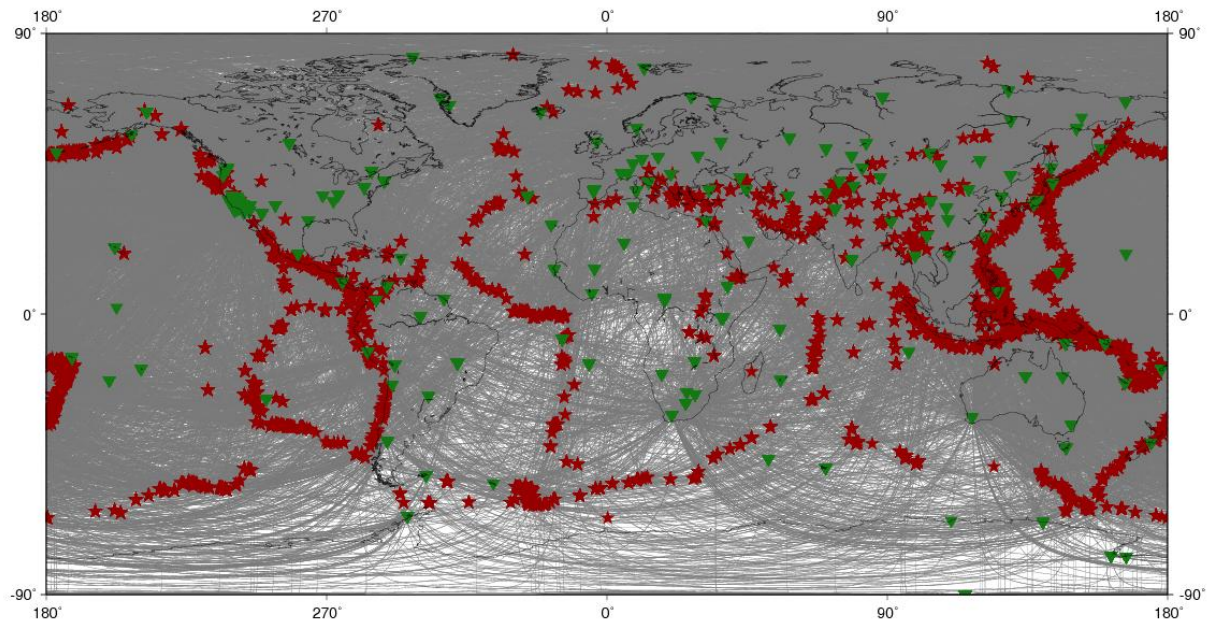


**Figure 8.** Inversions for Love waves at 150 s period and input models of 2% perturbations and different scalelengths of heterogeneities: (a) checkerboard defined as a single spherical harmonic of degree  $l = 9$  and order  $m = 5$ , (b) checkerboard with  $l = 13$  and  $m = 7$  and (c) checkerboard with  $l = 20$  and  $m = 10$ . The input models are shown in the left column, solutions of the ray-theoretical inversions in the middle and finite-frequency inversions on the right column.

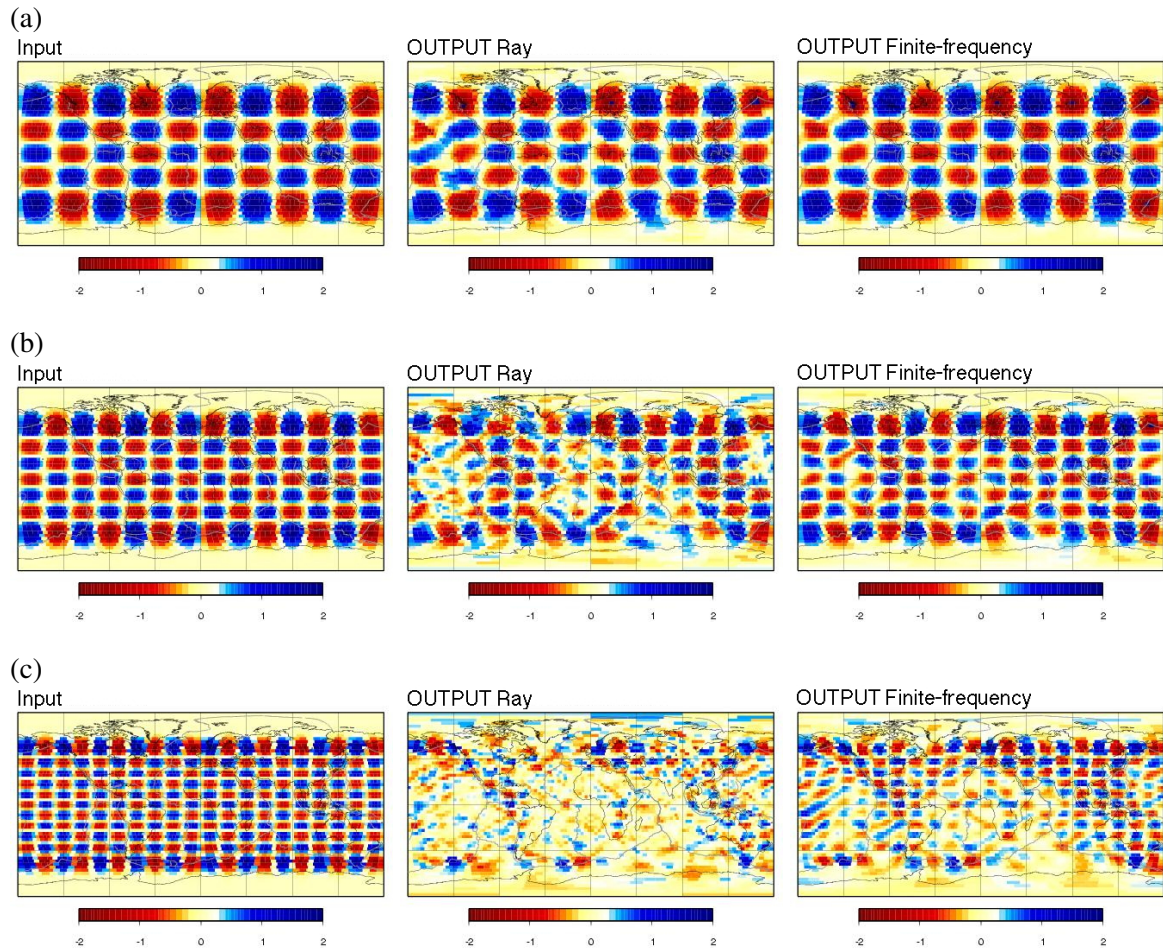


**Figure 9.** Inversions for Love waves at 100 s period and input models of 2% perturbations and different scalelengths of heterogeneities: (a) checkerboard with spherical harmonic degree  $l = 13$  and  $m = 7$  and (b) checkerboard with  $l = 20$  and  $m = 10$ . The input models are shown in the left column, solutions of the ray-theoretical inversions in the middle and finite-frequency inversions on the right column.

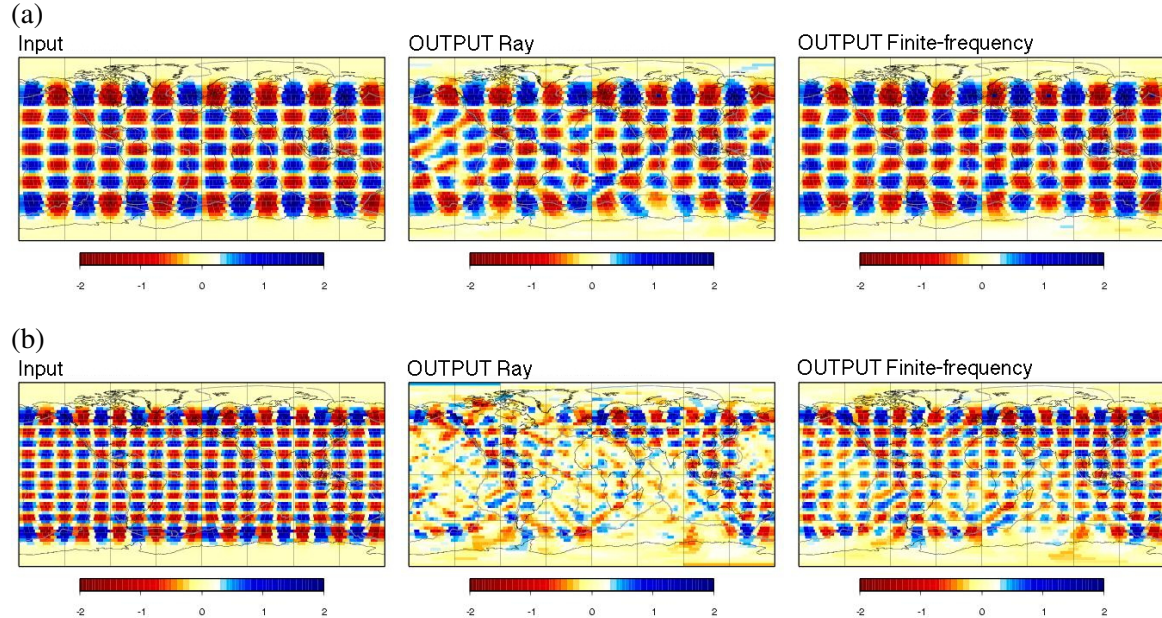


**Figure 10.** Using statistical noise in the synthetic dataset, solutions for Love waves at 150 s period and an input model of 2% perturbations are shown: (a) with a checkerboard with  $l = 13$  and  $m = 7$  and (b) with a checkerboard with  $l = 20$  and  $m = 10$ . The input models are shown in the left column, solutions of the ray-theoretical inversions in the middle and finite-frequency inversions on the right column.

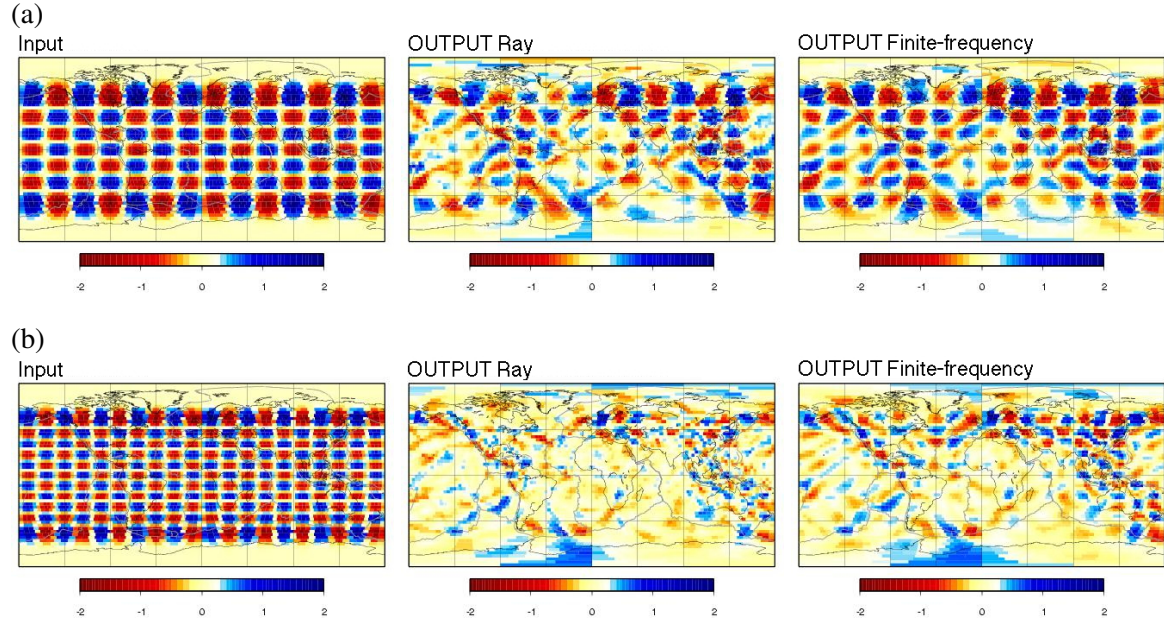


**Figure 11.** Influence of large amplitude of heterogeneities. Solutions are shown for Love waves at 150 s period and an input model of (a) 10% perturbations with a checkerboard with  $l = 9$  and  $m = 5$ . On the left, the input model is shown, while in the middle and on the right side the ray-theoretical and finite-frequency solutions, respectively, are plotted. The power spectrum up to spherical harmonic degree 25 is shown of the ray-theoretical solution image in (b) as red bars, the corresponding one of the finite-frequency solution image in (c), both plotted against the initial power spectrum of the input model (black box).

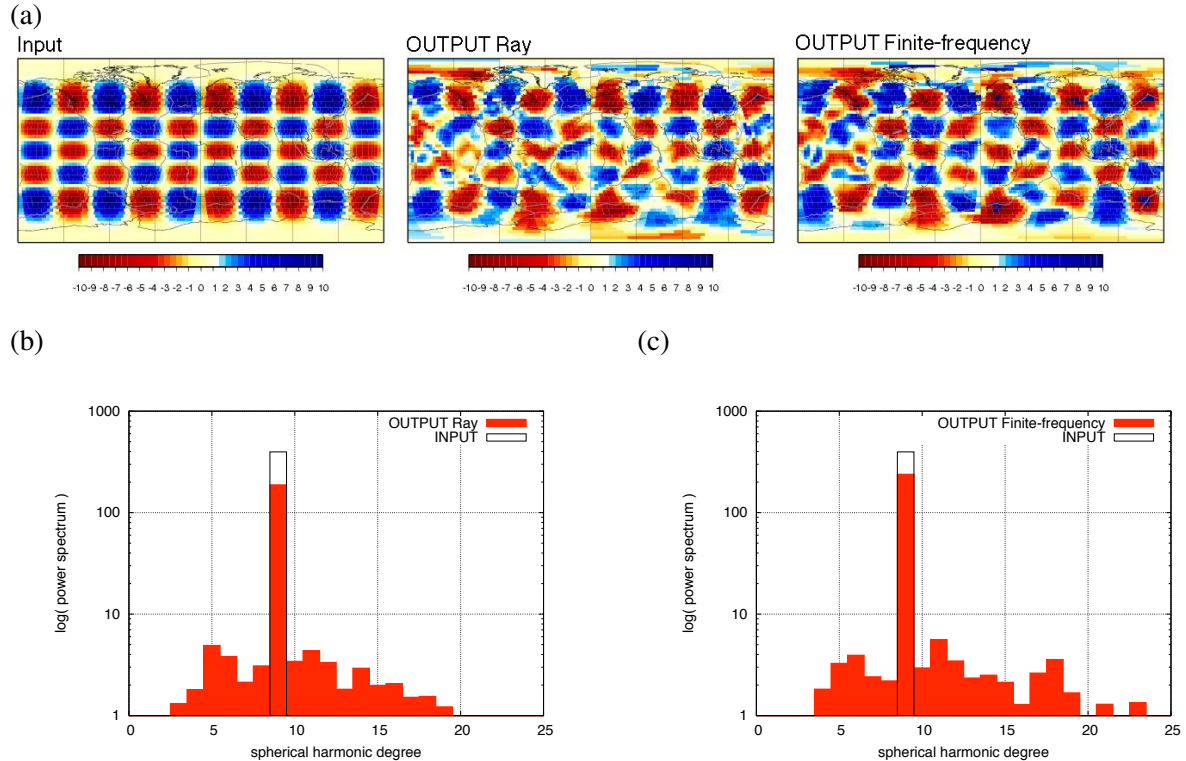


**Figure 12.** Realistic input model TW96 solved for Love waves at 150 s period. (a) The input model is shown on the left, the ray-theoretical inversion in the middle and the finite-frequency inversion solution on the right. The corresponding power spectrum up to spherical harmonic degree 25 of (b) the ray-theoretical solution image (red bars) and (c) the finite-frequency solution image (red bars) are plotted against the initial power spectrum of the input model (black boxes).

